

Irreversible Response of the Intertropical Convergence Zone (ITCZ) to CO₂ Forcing

Jong-Seong Kug (✉ jskug1@gmail.com)

Pohang University of Science and Technology

Ji-Hoon Oh

Pohang University of Science and Technology <https://orcid.org/0000-0001-8484-8997>

Soon-Il An

Yonsei University <https://orcid.org/0000-0002-0003-429X>

Seung-Ki Min

Pohang University of Science and Technology <https://orcid.org/0000-0002-6749-010X>

Sang-Wook Yeh

Hanyang University

Seok-Woo Son

Seoul National University

Jong-Hoon Kam

Pohang University of Science and Technology

Yoo-Geun Ham

Chonnam National University

Jongsoo Shin

Yonsei University

Article

Keywords: CO₂ Ramp Up and Down Experiments, Irreversible Precipitation Changes, El Nino-like Pattern, Global Hydrological Cycle, Atlantic Meridional Overturning Circulation, Delayed Energy Exchanges

Posted Date: March 11th, 2021

DOI: <https://doi.org/10.21203/rs.3.rs-241280/v1>

License:  This work is licensed under a Creative Commons Attribution 4.0 International License.

[Read Full License](#)

Version of Record: A version of this preprint was published at Nature Climate Change on December 9th, 2021. See the published version at <https://doi.org/10.1038/s41558-021-01211-6>.

17 **Introductory paragraph**

18 **With the unprecedented rate of global warming in this century, whether or**
19 **not human-made climate change is irreversible is the most critical question. Based**
20 **on idealized CO₂ ramp-up and -down experiments, we show here that the**
21 **intertropical convergence zone (ITCZ) exhibits irreversible changes. While the**
22 **ITCZ location does not change much during the CO₂ increasing period, the ITCZ**
23 **sharply moves south as soon as CO₂ begins to decrease, and its center eventually**
24 **resides in the Southern Hemisphere. The pattern of the irreversible precipitation**
25 **changes manifests a permanent extreme El Nino-like pattern, which has distinctive**
26 **impacts on the global hydrological cycle. It was revealed that the hysteresis behavior**
27 **of the Atlantic meridional overturning circulation and the delayed energy exchanges**
28 **between the tropics and extratropics are responsible for the peculiar evolution of the**
29 **hemispheric temperature contrast, leading to irreversible ITCZ changes.**

30
31 Earth's climate has continuously been changing, but the current global warming
32 speed is unprecedented, at least during the last 22,000 years¹. Such unprecedented change
33 has raised a concern that our climate may cross a critical threshold. It has been widely
34 accepted that our Earth climate system has experienced large abrupt and irreversible
35 changes in the past when Earth's climate system crossed certain thresholds²⁻⁵. However,
36 it is unclear whether or not anthropogenic climate changes will be reversible. If they are
37 not reversible, understanding which climate components are irreversible is most critical.
38 Here the reversibility indicates whether Earth's climate system or an individual climate

39 component can be returned to its original state within a certain period if the greenhouse
40 gases in the atmosphere are reduced.

41 So far, climate reversibility and hysteresis have been investigated using climate
42 models with idealized forcing scenarios⁶⁻¹⁵. It was suggested that the temperature and
43 precipitation responses to the increased greenhouse gases are largely reversible within a
44 century from the global mean perspective^{12,15}. However, several key components in the
45 earth system are expected to exhibit irreversible and hysteresis behaviors, such as the sea-
46 level rise, ocean acidification¹², Atlantic meridional overturning circulation (AMOC)¹⁵,
47 and the global/regional hydrological cycle⁷. Particularly, understanding the irreversible
48 and hysteresis behaviors of hydrological cycles is crucial for climate adaptation and
49 mitigation policies.

50 Tropical rainfall is concentrated in a narrow band known as the intertropical
51 convergence zone (ITCZ), which accounts for 32% of the global precipitation¹⁶. The
52 zonally-elongated intense ITCZ rainfall is maintained by strong low-level convergence,
53 which leads to strong ascending motion, resulting in the meridional overturning Hadley
54 circulation. Thus, slight changes in the ITCZ rainfall can have tremendous impacts on
55 global climate^{17,18}. As it seasonally migrates toward the warmer hemisphere, the ITCZ
56 meridionally migrates when hemispheric asymmetry of the temperature changes by
57 altering the interhemispheric atmospheric heat flux¹⁹⁻²⁴.

58 Anthropogenic global warming influences the location, width, and intensity of the
59 ITCZ²⁵⁻²⁸, ultimately leading to regional climate changes. Current climate models
60 simulate the ITCZ narrowing but reduced its strength under greenhouse warming^{25,27}.
61 However, future changes in the ITCZ location are uncertain²⁷, so more attention is

62 needed. The main overarching questions in this study are as follows. Is the ITCZ change
63 reversible? What determines irreversibility? How does this irreversibility affect
64 global/regional hydrological cycles?

65 To examine climate reversibility, we conducted an idealized CO₂ ramp-up and -
66 down experiment. In this experiment, the atmospheric CO₂ concentration was gradually
67 increased up to four times the present level and then reduced at the same rate to the
68 present level (see Methods and Fig. 1a). To get robust results, a total of 28 ensemble
69 simulations were conducted with different initial conditions.

70

71 **Hysteresis behavior for temperature, precipitation, and ITCZ location**

72 Figure 1a shows the global mean temperature response to the ramp-up and -down
73 forcing. The temperature increased by ~5K when the CO₂ became four times the present
74 level. The temperature evolution was largely corresponding to the CO₂ changes, suggesting
75 a reversible response, though the peak was delayed for some years^{7,13}. Note that the
76 temperature in 2280 was ~1K higher than in the present state although the CO₂ was
77 returned to its original value. Though the maximum global mean precipitation appeared to
78 be several years more delayed compared with the temperature, the overall evolution
79 followed the temperature evolution well to a large extent, suggesting that the global mean
80 precipitation response is roughly reversible.

81 However, the regional hydrological cycles show quite different behaviors.
82 Particularly, the ITCZ precipitation and its distribution shows a peculiar evolution in
83 response to the CO₂ ramp-up and -down forcing. To measure the ITCZ latitudinal
84 migration, we adopted an ITCZ centroid index, which is defined as the median of the zonal-

85 mean precipitation in the tropics^{21,22,29} (see Methods). As the CO₂ increased in the ramp-
86 up period, the ITCZ centroid did not change much. Surprisingly, however, as soon as the
87 CO₂ began to decrease, the ITCZ centroid sharply moved south, and it continuously
88 migrated until ~2230. Thus, the ITCZ centroid was even shifted to the Southern
89 Hemisphere (SH). After that, the ITCZ slowly moved back north, but it was still located in
90 the SH even after the CO₂ concentrations returned to the present level. When the model
91 was integrated 220 years more with the present CO₂ level, the ITCZ centroid moved back
92 north in the early 100 years but still resided far from the original location (Extended Data
93 Fig. 1). This result suggests that the ITCZ response to the CO₂ forcing is largely irreversible.

94 The hysteresis behaviors of the climate system in the present model experiment are
95 shown in Fig. 1c-e. The global mean temperature shows a nearly linear response to the CO₂
96 concentration, indicating a weak hysteresis behavior. The precipitation shows a hysteresis
97 behavior to some extent^{7,8,13}. However, the ITCZ centroid shows a clearer hysteresis
98 behavior. The location is mostly southward on the CO₂ ramp-down pathway, and it remains
99 quite far from the original position by the time CO₂ returns to the initial value.

100

101 **Tropical hydrological cycle responses to the ramp-up and -down CO₂ forcing**

102 To understand the irreversible changes of the ITCZ, Fig. 2a shows changes in the
103 zonal-mean precipitation over time. To emphasize an asymmetric response to the
104 symmetric CO₂ pathway, we calculated the difference between the precipitations in each
105 year and the mean precipitation at the CO₂ peak phase (Year 2135–2145). During the ramp-
106 up period, the equatorial rainfall considerably increased, but the off-equatorial rainfall
107 decreased in both hemispheres, suggesting the so-called narrowing ITCZ^{25,27,30} (Extended

108 Data Fig. 2), which is related to the enhanced equatorial warming^{31,32}. The equatorial
109 rainfall further increased for ~10 years after the CO₂ forcing turnabout point, but it
110 gradually decreased until the CO₂ returned to its initial value. The off-equatorial rainfall in
111 the Northern Hemisphere (NH) continuously decreased despite the decrease in the CO₂,
112 showing an asymmetric behavior. The off-equatorial rainfall in the SH started to increase
113 from the CO₂ peak time, indicating a symmetric behavior to some extent. However, the
114 increasing rate in the ramp-down phase was explosive, so the rainfall became larger than
115 that of any period of the ramp-up phase. The maximum rainfall difference in the SH off-
116 equatorial region (5°S–15°S) appeared in Year 2235, which is five times larger than that
117 of the present climate (Year 2000). The decreasing trend in the NH and increasing trend in
118 the SH indicate a distinctive southward shift of the ITCZ.

119 Figure 2b shows the difference in the annual mean precipitation between Year 2210
120 and 2070 when the CO₂ concentrations were identically double the present level. Though
121 the CO₂ radiative forcing is the same, the two periods showed profound differences in the
122 precipitation patterns. First, the precipitation increased in the SH tropics and decreased in
123 the NH tropics, indicating the southward shift of the ITCZ. Such hemispheric contrast is
124 consistently evident over all the Indian, Pacific, and Atlantic basins, suggesting that the
125 southward shift is caused by a global-scale change. Interestingly, in the tropical Pacific
126 region, increased precipitation was also manifested in the equatorial eastern and central
127 Pacific, so the pattern in the tropical Pacific is similar to that during the extreme El Nino
128 (Extended Data Fig. 3). This suggests that the global climate in the ramp-down phase may
129 experience anomalous conditions similar to those of a persistent extreme El Nino period.
130 It was also noted that there is a hemispheric contrast in high latitudes. While the

131 precipitation increased in the Southern Ocean, a distinctive decrease was evident in the NH
132 subpolar Atlantic Ocean, which can be possibly related to the AMOC change³³⁻³⁵.

133 The precipitation pattern shown in Fig. 2b is from the single model result and might
134 be model-dependent. To show the robustness of the ITCZ response, we also analyzed six
135 model simulations from the Coupled Model Intercomparison Project Phase 6 (CMIP6)
136 archives³⁶ (see Methods). As shown in Fig. 2c and Extended Data Fig. 4, considering the
137 tropical precipitation difference, the most models show essentially the same pattern as the
138 result of the present experiment. As well as the pattern, the temporal evolution was also
139 similar (Extended Data Fig. 5). This suggests that the pattern of the tropical precipitation
140 change is not model-dependent.

141 The precipitation changes were closely related to the temperature changes. Since
142 the global mean temperature was higher in the ramp-down period, overall warming was
143 evident in the tropics and SH extratropics (Fig. 2d). Particularly, the Southern Ocean and
144 tropical eastern Pacific warming were more distinctive, where the precipitation was largely
145 increased (Fig. 2b). However, it is remarkable that the strongest cooling is in the NH
146 subpolar Atlantic regions despite the higher global mean temperature. This temperature
147 pattern resembles temperature anomalies in the AMOC weakened phase^{34,35}. Since the
148 hemispheric temperature contrast was evident, the ITCZ is expected to move toward the
149 warmer hemisphere^{35,37-39}.

150 To understand the precipitation changes, the moisture flux was calculated (Fig. 2e
151 and Extended Data Fig. 5). Warming was highest in the Southern Ocean, but in the zonal-
152 mean perspective, there were negligible moisture supplies from the SH extratropics into
153 the SH ITCZ zone, where the precipitation was significantly increased. Instead, the

154 intensified ITCZ precipitation in the SH was mostly contributed by the cross-equatorial
155 moisture flux, which is associated with the southward shift of the rising branch in the
156 Hadley circulation. Also, a strong moisture convergence is found in the subpolar North
157 Atlantic, where the precipitation was considerably decreased, possibly due to the extremely
158 reduced evaporation.

159

160 **Irreversible ITCZ responses and global energy exchanges**

161 Though we showed that the southward shift of the ITCZ is maintained by
162 the cross-equatorial moisture flux, this can be interpreted as a result of the coupling
163 between the ITCZ and the overturning Hadley circulation rather than the cause of the
164 southward shift. The difference in the hemispheric temperature distribution (Fig. 2d), can
165 be responsible for the distinct ITCZ responses to the same CO₂ forcing. Thus, we introduce
166 an energy flux equator (see Methods), which is defined as the latitude at which the zonal-
167 mean atmospheric meridional energy flux changes the sign^{37,40}. Since the energy flux
168 equator mostly corresponds to the rising branch of the Hadley circulation, it is also closely
169 related to the latitudinal location of the ITCZ. Therefore, the ITCZ location was roughly
170 proportional to the sign and strength of the cross-equatorial energy flux^{37,40}. For example,
171 the negative (positive) cross-equatorial energy flux indicates the energy flux equator and
172 the located ITCZ in the NH (SH). In the present climate, the atmospheric energy flux at the
173 equator is negative, and the energy flux equator is located at ~2.8°N (Fig. 3a). With the
174 increase in CO₂, the cross-equatorial energy flux slowly increased, and the energy flux
175 equator slightly migrated south, in part due to the narrowing ITCZ (Fig. 3a and Extended
176 Data Fig. 2). In Year 2070, the energy flux equator was ~2°N. After the turnabout of the

177 CO₂ forcing, the cross-equatorial flux began to sharply increase, and its sign was even
178 changed, indicating that the center of the ITCZ moved to the SH. In Year 2210, the flux
179 equator was located at ~1.5°S.

180 The cross-equatorial energy flux is related to the tropospheric temperature
181 distribution in the tropics^{35,37-39}. Figure 3b shows a vertically integrated temperature
182 difference in the tropics between the NH and SH (see Methods). Due to the continental
183 distribution and existence of the coldest Antarctic continent, the NH was warmer than the
184 SH, leading to a positive interhemispheric temperature difference in even the tropics. With
185 the increase in CO₂, the temperature difference was expected to increase because
186 continental warming is usually faster than the ocean. Interestingly, however, the
187 temperature difference did not change much during the ramp-up period (Fig. 3b). As soon
188 as the CO₂ decreased, the temperature difference rapidly decreased, indicating that the
189 decrease in the NH temperature is faster than in the SH temperature. Since Year 2230, the
190 temperature difference was flattened.

191 It is striking that the tropospheric temperature difference evolution was quite
192 similar to that of the ITCZ centroid and maximum zonal-mean precipitation region. This
193 shows that the hemispheric temperature contrast is closely related to the peculiar evolution
194 of the ITCZ, which is clearly far from the CO₂ evolution. These changes in the
195 interhemispheric temperature distribution are largely attributed to the competition between
196 the contributions of the NH continent and SH Oceanic warming (Extended Data Fig. 6).
197 For example, the slower decrease in the SH tropical temperature can result from two factors.
198 First, the SH tropics are covered by more ocean surface, leading to slower cooling. More
199 importantly, the heat exchange between the tropics and extratropics over the SH can

200 contribute to slower cooling. As shown in Fig. 2d, during the ramp-down period, the
201 highest warming was manifested in the Southern Ocean, which plays a role in reducing the
202 poleward heat transfer to the SH extratropics (Fig. 3c), contributing to warming in the SH
203 tropics. This contradicts the increasing poleward heat transport in the NH (Fig. 3c). The
204 Southern Ocean warming is partly due to its large heat storage⁴¹. Additionally, the AMOC
205 is a key driver for the Southern Ocean warming and NH Atlantic cooling.

206 Figure 3c shows the AMOC response to the CO₂ ramp-up and -down forcing. With
207 the increase in CO₂, the overturning circulation was gradually weakened due to the
208 freshening of the Arctic sea-ice decline⁴², the buoyant surface cap⁴³, and surface hydrology
209 change⁴⁴. After the CO₂ turnabout, the AMOC strength further weakened and reached its
210 minimum value in about Year 2200, namely the AMOC overshooting (Extended Data Fig.
211 1) due to the salinity build-up in the subtropical Atlantic during the ramp-up phase⁴⁵.
212 Afterward, the AMOC strength started to rapidly recover. As described in the previous
213 studies^{15,43,45}, the AMOC exhibits a clear hysteresis behavior, and such behavior has critical
214 influences on the ITCZ changes due to the alterations in the hemispheric heat distribution.

215 In the ramp-up phase, the AMOC weakening induced SH warming and NH cooling,
216 which offset the faster continental warming in the NH, so the hemispheric temperature
217 difference could be flat (Fig. 3b). After the CO₂ forcing turnabout, the AMOC was still
218 weakening, and the decrease in CO₂ forcing led to the oceanic cooling being slower than
219 the continental cooling, resulting in slower cooling in the SH. By combining these two
220 effects, the hemispheric difference could rapidly decrease (Fig. 3b), leading to the sharp
221 southward shift in the ITCZ. As the AMOC strength began to recover at about Year 2200,
222 it compensated for the slower oceanic cooling, so the hemispheric temperature difference

223 looks flattened in this period. Therefore, the southward-shifted ITCZ did not come back
224 shortly, implying the irreversible response of the ITCZ. Note that there was a time delay
225 of a couple of decades between the minimum AMOC and tropical temperature difference,
226 which might be interpreted as the time to adjust to the temperature redistribution from the
227 extratropics to the tropics by the energy exchanges. For instance, the energy flux at 30°S
228 was still decreasing until Year 2280, contributing to the slower cooling in the SH tropics
229 and holding the ITCZ in the SH.

230 In summary, we here suggest that the hysteresis response of the deep ocean
231 circulation and time-delayed responses between the continental and oceanic surface to the
232 CO₂ forcing can lead to the peculiar evolution of the hemispheric temperature contrast. The
233 resultant energy exchanges between the two hemispheres and between the tropics and
234 extratropics were found to result in an irreversible change in the ITCZ. Such change might
235 be eventually returned to the original state if the present CO₂ forcing is continuously
236 prescribed, but it is not expected to take place within a couple of centuries (Extended Data
237 Fig. 1). Also, in the stabilization period, the precipitation change intensity was weakened,
238 but the spatial pattern was maintained (Extended Data Fig. 7).

239

240 **Impacts of the irreversible ITCZ responses on the regional hydrological cycles**

241 Though most of the ITCZ precipitation takes place over the ocean, its change has
242 tremendous impacts on the global hydrological cycle by modulating the zonal and
243 meridional overturning circulations^{17,18,33}. Figure 4 shows the annual mean land
244 precipitation difference between 2210 and 2070. As the ITCZ moved southward, most of
245 the tropical lands in the NH were drier. Particularly, the arid conditions in the Sahara Desert

246 and its surrounding areas, Sahel Zone, and the semi-arid conditions around the
247 Mediterranean Sea deteriorated even though the CO₂ concentration returned to its original
248 value (Fig. 4b). However, precipitation in the extratropical Northern and Southern
249 Americas increased in the ramp-down phase. It is conceived that these changes are related
250 to the precipitation pattern, which is similar to the permanent extreme El Nino period,
251 leading to heating-induced teleconnections (Extended Data Fig. 3). Particularly, the arid
252 area in the western coastal area of North America greatly became moist, implying that this
253 region is one of the most beneficial regions for decarbonization or carbon removal. The
254 Antarctica precipitation largely increased due to the warmer Southern Ocean and the
255 resultant moisture flux (Fig. 2e), which may help in recovering the Antarctic glaciers and
256 thus sea-level changes.

257 In this study, we conducted idealized climate experiments that provided insights
258 into a hypothetical scenario of carbon dioxide removal, which must be taken into account
259 when assessing the implications of various mitigation options for flooding, water supply,
260 food production, and human health. Also, we here showed that the ITCZ and global
261 hydrological cycle can be changed into a different state or be recovered much later than
262 expected even if we successfully managed to reduce the CO₂ concentration. Such
263 irreversible and hysteresis behaviors are incurred because the global hydrological cycle is
264 a combined result of complex climate components that have quite different adjustment
265 timescales in response to anthropogenic climate forcing. While the global mean
266 temperature was widely used for measuring climate risks, our study showed that the global
267 mean temperature alone is a poor metric to measure any changes in our climate system.
268 Additionally, we showed that the evolution of the global hydrological cycle is quite

269 different from that of the global mean temperature. Finally, our study showed that the CO₂
270 influences, which have already taken place, will persist for a longer time than expected and
271 that future CO₂ emission will bring about further irreversible effects. Thus, a climate
272 mitigation policy must be taken into account not only for reducing the damages of
273 immediate climate changes but also to prevent or even reduce the expected irreversible
274 long-term changes.

275 **METHODS**

276 **Dataset used and experimental design**

277 To investigate the irreversible ITCZ responses to CO₂ ramp-up and -down forcing,
278 we conducted experimental climate model simulations. The model used in this study is a
279 fully-coupled Community Earth System Model version 1.2.2, which has the same
280 component models and coupling of the CESM1 with the Community Atmosphere Model
281 version 5 (CAM5) in CMIP5^{46,47}. The atmosphere and land components used a horizontal
282 resolution of $\sim 1^\circ$ with 30 vertical levels. The ocean and sea-ice components used a nominal
283 1° horizontal resolution (meridional resolution is $\sim 1/3^\circ$ near the equator) with 60 vertical
284 levels in the ocean.

285 We performed two kinds of simulations. One is a present-day run (PD) with a
286 constant CO₂ concentration ($1\times\text{CO}_2$, 367 ppm) of over 900 years, where we extracted 28
287 initial conditions from the PD run. Also, a CO₂ ramp-up and -down experiment was
288 performed. This experiment employed an increasing atmospheric CO₂ concentration at a
289 rate of $1\% \text{ year}^{-1}$ until CO₂ quadrupling ($4\times\text{CO}_2$, 1478 ppm) and then a decreasing CO₂
290 forcing to the same rate over 140 years until reaching the original value ($1\times\text{CO}_2$, 367 ppm).
291 Additionally, we integrated a restoring run of 220 years with a constant CO₂ concentration
292 ($1\times\text{CO}_2$, 367 ppm).

293 Moreover, the irreversible ITCZ responses to the CO₂ ramp-up and -down forcing
294 were examined using six models from the CMIP6³⁶ (List of the used models: ACCESS-
295 ESM1-5, CanESM5, CESM2, MIROC-ES2L, UKESM1-0-LL, GFDL-ESM4). We used
296 the dataset of the 1pctCO₂ scenario from the CMIP6 Diagnostic, Evaluation, and
297 Characterization of Klima (DECK)³⁶ and the 1pctCO₂-cdr scenario from the Carbon

298 Dioxide Removal MIP (CDRMIP)⁴⁸. The experimental setup is quite similar to our
299 simulations except for the initial CO₂ concentration level (pre-industrial level, 284.7 ppm).
300 These data were used after it was re-gridded to a 1° × 1° horizontal resolution.

301

302 **Definition of indices**

303 1. ITCZ centroid^{21,22,29} is defined as the median of the zonal-mean precipitation in the
304 tropics (from 20°S to 20°N), which means the latitude dividing the annual and zonal-mean
305 precipitation equally in half. The precipitation data is interpolated to a 0.1° grid over the
306 tropics to resolve the ITCZ centroid at increments smaller than the original grid spacing.

307 2. Interhemispheric temperature contrast is defined as the difference between the tropics
308 (0°–30°N and 30°S–0) of the NH and SH annual mean temperature, which is vertically
309 averaged from the surface to 300hPa.

310 3. AMOC strength is defined as the average of the annual mean Atlantic meridional ocean
311 stream function from 35°N to 45°N at a depth of 1000 m (climatological maximum position
312 in the PD).

313

314 **Atmospheric meridional energy flux**

315 To examine the energy flux equator to approximately follow the ITCZ location, we
316 calculated the atmospheric moist static energy flux using atmospheric energy budgets. As
317 in the previous studies^{37,40,49}, the energy budgets of a whole atmospheric column can be
318 denoted as:

$$\frac{\partial E_A}{\partial t} = S - L - O - \nabla \cdot \bar{F}, \quad (1)$$

319 where $\frac{\partial E_A}{\partial t}$ is the time tendency of the atmospheric energy storage (Wm^{-2}), and S, L
 320 denote the net incoming shortwave and longwave radiation values (Wm^{-2}) at the top of
 321 the atmosphere, respectively. O is the ocean heat uptake (Wm^{-2}) (or generally the net
 322 surface energy budget), and \bar{F} is the vertically integrated zonal and annual mean of the
 323 meridional atmospheric moist static energy flux (Wm^{-1}).

324 The atmospheric energy storage can be written as:

$$E_A = \frac{1}{g} \int_0^{p_s} (c_p T + k + L_v q + \Phi_s) dp, \quad (2)$$

325 where g is the gravitational acceleration (ms^{-2}), c_p is the specific heat of the atmosphere
 326 at constant pressure ($JK^{-1}kg^{-1}$), T is the temperature (K), k is the kinetic energy
 327 (Jkg^{-1}), which is neglected here due to the relatively small amplitude⁴⁹, L_v is the latent
 328 heat of vaporization (Jkg^{-1}), q is the specific humidity ($kgkg^{-1}$), Φ_s is the surface
 329 geopotential energy (m^2s^{-2}), which is not related with pressure⁴⁹, p is the pressure (Pa),
 330 and p_s is the surface pressure.

331 Now, integrating equation (1) with the latitudinal weighting from the South Pole
 332 ($\phi = -\frac{\pi}{2}$) to a certain latitude (ϕ) and all the longitudes in the spherical coordinates results
 333 in:

$$F(\phi) = \int_{-\frac{\pi}{2}}^{\phi} 2\pi a^2 \cos\phi \left(S - L - O - \frac{\partial E_A}{\partial t} \right) \partial\phi, \quad (3)$$

334 where the atmospheric meridional energy flux F has a unit W , as in Fig. 3a.

335

336 **Acknowledgments**

337 This work was supported by the National Research Foundation of Korea (NRF-
338 2018R1A5A1024958), the National Supercomputing Center with supercomputing
339 resources including technical support (KSC-2018-CHA-0062), and the Korea Research
340 Environment Open NETwork (KREONET).

341

342 **Author contributions**

343 J.-H. Oh compiled the data, conducted analyses, prepared the figures, and wrote the
344 manuscript. J.-S. Kug designed the research and wrote majority of the manuscript content.
345 All of the authors discussed the study results and reviewed the manuscript.

346

347 **Data availability**

348 Processed model data will be available on the server, <https://www.yonseiircc.com/>, and the
349 CMIP6 archives are freely available from <https://esgf-node.llnl.gov/projects/cmip6/>.

350

351 **Code availability**

352 Processed data, products, and code produced in this study are available from the
353 corresponding author upon reasonable request.

354

355 **Correspondence and requests for materials** should be addressed to J.-S. Kug
356 (jskug@postech.ac.kr).

357

358 **References**

- 359 1. Joos, F. & Spahni, R. Rates of change in natural and anthropogenic radiative
360 forcing over the past 20,000 years. *Proc. Natl. Acad. Sci. U. S. A.* **105**, 1425–1430
361 (2008).
- 362 2. Miller, G. H. *et al.* Abrupt onset of the Little Ice Age triggered by volcanism and
363 sustained by sea-ice/ocean feedbacks. *Geophys. Res. Lett.* **39**, 1–5 (2012).
- 364 3. Renaud, F. G. *et al.* Tipping from the Holocene to the Anthropocene: How
365 threatened are major world deltas? *Curr. Opin. Environ. Sustain.* **5**, 644–654
366 (2013).
- 367 4. Broecker, W. S. Unpleasant surprises in the greenhouse? *Futur. Nat. Doc. Glob.*
368 *Chang.* 337–347 (2013).
- 369 5. Thornalley, D. J. R. *et al.* Anomalously weak Labrador Sea convection and
370 Atlantic overturning during the past 150 years. *Nature* **556**, 227–230 (2018).
- 371 6. Tsutsui, J. *et al.* Long-term climate response to stabilized and overshoot
372 anthropogenic forcings beyond the twenty-first century. *Clim. Dyn.* **28**, 199–214
373 (2007).
- 374 7. Wu, P., Wood, R., Ridley, J. & Lowe, J. Temporary acceleration of the
375 hydrological cycle in response to a CO₂ rampdown. *Geophys. Res. Lett.* **37**, 1–5
376 (2010).
- 377 8. Cao, L., Bala, G. & Caldeira, K. Why is there a short-term increase in global
378 precipitation in response to diminished CO₂ forcing? *Geophys. Res. Lett.* **38**, 1–6
379 (2011).
- 380 9. Gillett, N. P., Arora, V. K., Zickfeld, K., Marshall, S. J. & Merryfield, W. J.
381 Ongoing climate change following a complete cessation of carbon dioxide
382 emissions. *Nat. Geosci.* **4**, 83–87 (2011).
- 383 10. Chadwick, R., Wu, P., Good, P. & Andrews, T. Asymmetries in tropical rainfall

- 384 and circulation patterns in idealised CO₂ removal experiments. *Clim. Dyn.* **40**,
385 295–316 (2013).
- 386 11. Lowe, J. A. *et al.* How difficult is it to recover from dangerous levels of global
387 warming? *Environ. Res. Lett.* **4**, (2009).
- 388 12. Frölicher, T. L. & Joos, F. Reversible and irreversible impacts of greenhouse gas
389 emissions in multi-century projections with the NCAR global coupled carbon
390 cycle-climate model. *Clim. Dyn.* **35**, 1439–1459 (2010).
- 391 13. Boucher, O. *et al.* Reversibility in an Earth System model in response to CO₂
392 concentration changes. *Environ. Res. Lett.* **7**, (2012).
- 393 14. Nohara, D., Yoshida, Y., Misumi, K. & Ohba, M. Dependency of climate change
394 and carbon cycle on CO₂ emission pathways. *Environ. Res. Lett.* **8**, (2013).
- 395 15. Wu, P., Ridley, J., Pardaens, A., Levine, R. & Lowe, J. The reversibility of CO₂
396 induced climate change. *Clim. Dyn.* **45**, 745–754 (2015).
- 397 16. Kang, S. M., Shin, Y. & Xie, S. P. Extratropical forcing and tropical rainfall
398 distribution: energetics framework and ocean Ekman advection. *npj Clim. Atmos.*
399 *Sci.* **1**, (2018).
- 400 17. Su, H. *et al.* Tightening of tropical ascent and high clouds key to precipitation
401 change in a warmer climate. *Nat. Commun.* **8**, 1–9 (2017).
- 402 18. Byrne, M. P. & Schneider, T. Atmospheric dynamics feedback: Concept,
403 simulations, and climate implications. *J. Clim.* **31**, 3249–3264 (2018).
- 404 19. Kang, S. M., Held, I. M., Frierson, D. M. W. & Zhao, M. The response of the
405 ITCZ to extratropical thermal forcing: Idealized slab-ocean experiments with a
406 GCM. *J. Clim.* **21**, 3521–3532 (2008).
- 407 20. Kang, S. M., Frierson, D. M. W. & Held, I. M. The tropical response to
408 extratropical thermal forcing in an idealized GCM: The importance of radiative

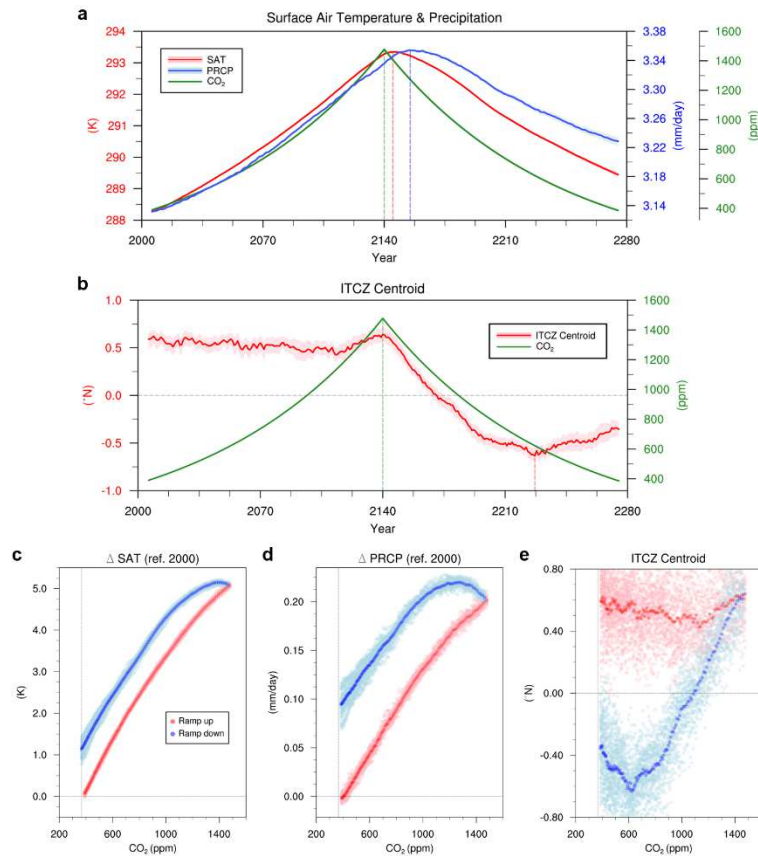
- 409 feedbacks and convective parameterization. *J. Atmos. Sci.* **66**, 2812–2827 (2009).
- 410 21. Frierson, D. M. W. & Hwang, Y. T. Extratropical influence on ITCZ shifts in slab
411 ocean simulations of global warming. *J. Clim.* **25**, 720–733 (2012).
- 412 22. Donohoe, A., Marshall, J., Ferreira, D. & Mcgee, D. The relationship between
413 ITCZ location and cross-equatorial atmospheric heat transport: From the seasonal
414 cycle to the last glacial maximum. *J. Clim.* **26**, 3597–3618 (2013).
- 415 23. Donohoe, A., Marshall, J., Ferreira, D., Armour, K. & Mcgee, D. The interannual
416 variability of tropical precipitation and interhemispheric energy transport. *J. Clim.*
417 **27**, 3377–3392 (2014).
- 418 24. Bischoff, T. & Schneider, T. The equatorial energy balance, ITCZ position, and
419 double-ITCZ bifurcations. *J. Clim.* **29**, 2997–3013 (2016).
- 420 25. Byrne, M. P. & Schneider, T. Narrowing of the ITCZ in a warming climate:
421 Physical mechanisms. *Geophys. Res. Lett.* **43**, 11,350–11,357 (2016).
- 422 26. Byrne, M. P. & Schneider, T. Energetic constraints on the width of the
423 intertropical convergence zone. *J. Clim.* **29**, 4709–4721 (2016).
- 424 27. Byrne, M. P., Pendergrass, A. G., Rapp, A. D. & Wodzicki, K. R. Response of the
425 Intertropical Convergence Zone to Climate Change: Location, Width, and
426 Strength. *Curr. Clim. Chang. Reports* **4**, 355–370 (2018).
- 427 28. Chou, C., Neelin, J. D., Chen, C. A. & Tu, J. Y. Evaluating the ‘rich-get-richer’
428 mechanism in tropical precipitation change under global warming. *J. Clim.* **22**,
429 1982–2005 (2009).
- 430 29. Moreno-Chamarro, E., Marshall, J. & Delworth, T. L. Linking ITCZ migrations to
431 the AMOC and North Atlantic/Pacific SST decadal variability. *J. Clim.* **33**, 893–
432 905 (2020).
- 433 30. Lau, W. K. M. & Kim, K. M. Robust Hadley circulation changes and increasing

- 434 global dryness due to CO₂ warming from CMIP5 model projections. *Proc. Natl.*
435 *Acad. Sci. U. S. A.* **112**, 3630–3635 (2015).
- 436 31. Liu, Z., Vavrus, S., He, F., Wen, N. & Zhong, Y. Rethinking tropical ocean
437 response to global warming: The enhanced equatorial warming. *J. Clim.* **18**, 4684–
438 4700 (2005).
- 439 32. Zhou, W., Xie, S. P. & Yang, D. Enhanced equatorial warming causes deep-
440 tropical contraction and subtropical monsoon shift. *Nat. Clim. Chang.* **9**, 834–839
441 (2019).
- 442 33. Lee, S.-Y., Chiang, J. C. H., Matsumoto, K. & Tokos, K. S. Southern Ocean wind
443 response to North Atlantic cooling and the rise in atmospheric CO₂: Modeling
444 perspective and paleoceanographic implications. *Paleoceanography* **26**, PA1214
445 (2011).
- 446 34. Liu, W., Fedorov, A. V., Xie, S. P. & Hu, S. Climate impacts of a weakened
447 Atlantic meridional overturning circulation in a warming climate. *Sci. Adv.* **6**, 1–9
448 (2020).
- 449 35. Cvijanovic, I. & Chiang, J. C. H. Global energy budget changes to high latitude
450 North Atlantic cooling and the tropical ITCZ response. *Clim. Dyn.* **40**, 1435–1452
451 (2013).
- 452 36. Eyring, V. *et al.* Overview of the Coupled Model Intercomparison Project Phase 6
453 (CMIP6) experimental design and organization. *Geosci. Model Dev.* **9**, 1937–1958
454 (2016).
- 455 37. Schneider, T., Bischoff, T. & Haug, G. H. Migrations and dynamics of the
456 intertropical convergence zone. *Nature* **513**, 45–53 (2014).
- 457 38. Friedman, A. R., Hwang, Y. T., Chiang, J. C. H. & Frierson, D. M. W.
458 Interhemispheric temperature asymmetry over the twentieth century and in future
459 projections. *J. Clim.* **26**, 5419–5433 (2013).

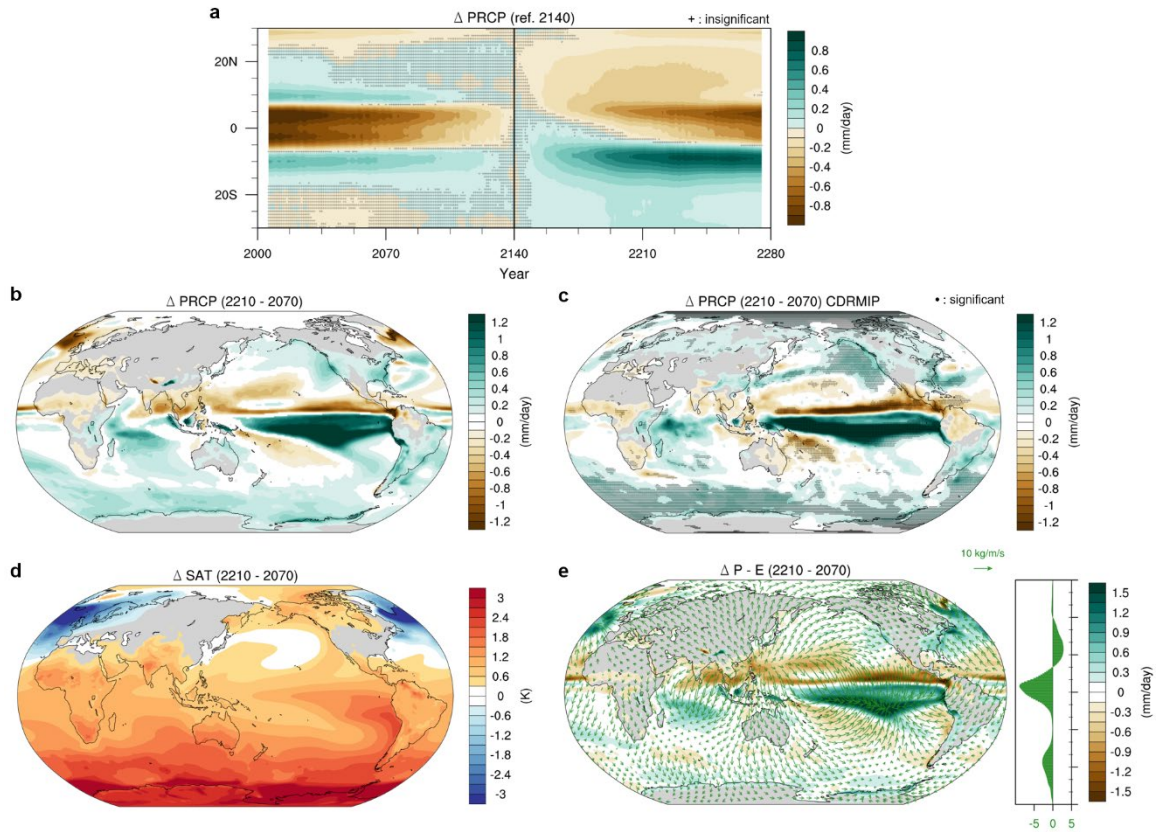
- 460 39. Chiang, J. C. H. & Bitz, C. M. Influence of high latitude ice cover on the marine
461 Intertropical Convergence Zone. *Clim. Dyn.* **25**, 477–496 (2005).
- 462 40. Bischoff, T. & Schneider, T. Energetic constraints on the position of the
463 intertropical convergence zone. *J. Clim.* **27**, 4937–4951 (2014).
- 464 41. Held, I. M. *et al.* Probing the fast and slow components of global warming by
465 returning abruptly to preindustrial forcing. *J. Clim.* **23**, 2418–2427 (2010).
- 466 42. Bakker, P. *et al.* Fate of the Atlantic Meridional Overturning Circulation: Strong
467 decline under continued warming and Greenland melting. *Geophys. Res. Lett.* **43**,
468 12,252–12,260 (2016).
- 469 43. Haskins, R. K., Oliver, K. I. C., Jackson, L. C., Wood, R. A. & Drijfhout, S. S.
470 Temperature domination of AMOC weakening due to freshwater hosing in two
471 GCMs. *Clim. Dyn.* **54**, 273–286 (2020).
- 472 44. Kim, H. & An, S.-I. On the subarctic North Atlantic cooling due to global
473 warming. *Theor. Appl. Climatol.* **114**, 9–19 (2013).
- 474 45. Jackson, L. C. Shutdown and recovery of the AMOC in a coupled global climate
475 model: The role of the advective feedback. *Geophys. Res. Lett.* **40**, 1182–1188
476 (2013).
- 477 46. Taylor, K. E., Stouffer, R. J. & Meehl, G. A. An overview of CMIP5 and the
478 experiment design. *Bull. Am. Meteorol. Soc.* **93**, 485–498 (2012).
- 479 47. Hurrell, J. W. *et al.* The community earth system model: A framework for
480 collaborative research. *Bull. Am. Meteorol. Soc.* **94**, 1339–1360 (2013).
- 481 48. Keller, D. P. *et al.* The Carbon Dioxide Removal Model Intercomparison Project
482 (CDRMIP): Rationale and experimental protocol for CMIP6. *Geosci. Model Dev.*
483 **11**, 1133–1160 (2018).
- 484 49. Fasullo, J. T. & Trenberth, K. E. The annual cycle of the energy budget. Part I:

485 Global mean and land-ocean exchanges. *J. Clim.* **21**, 2297–2312 (2008).

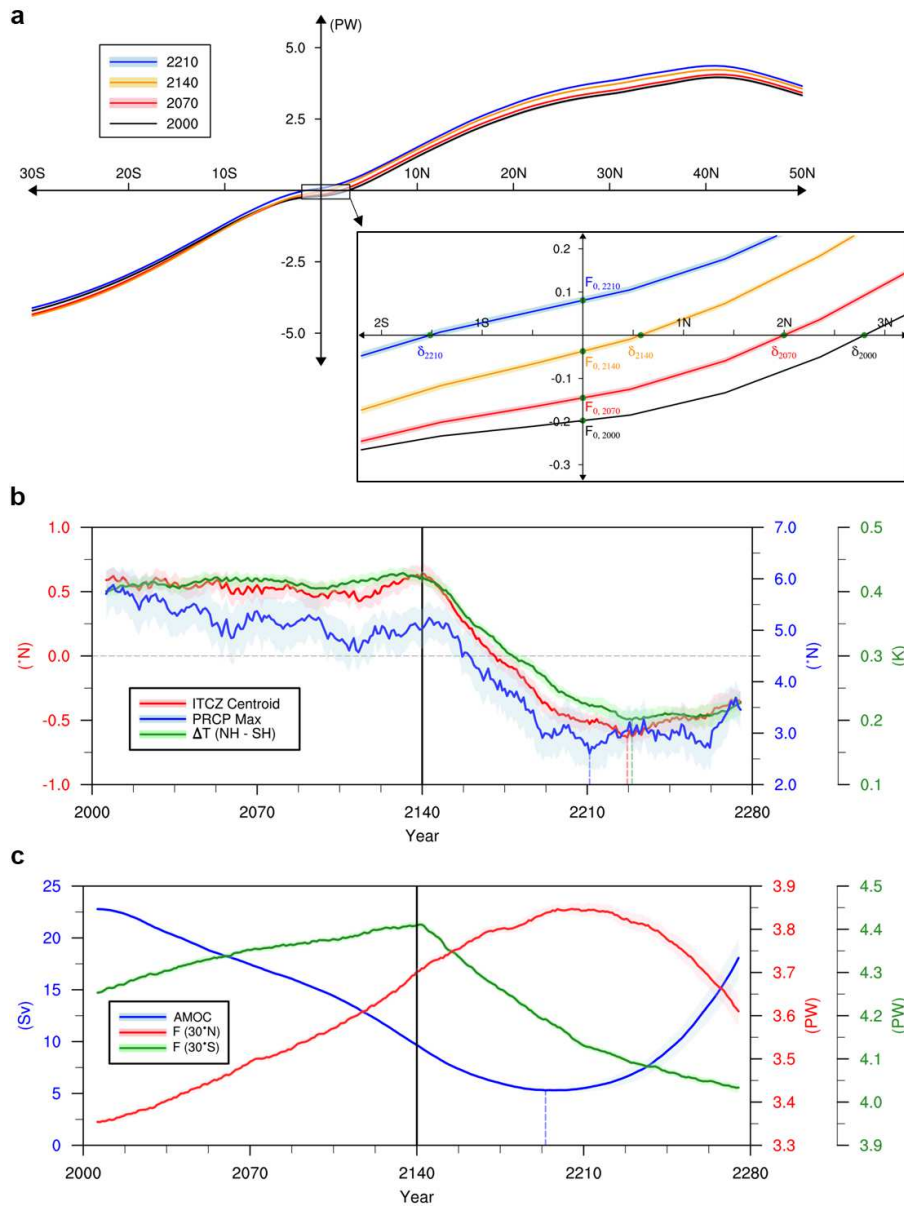
486



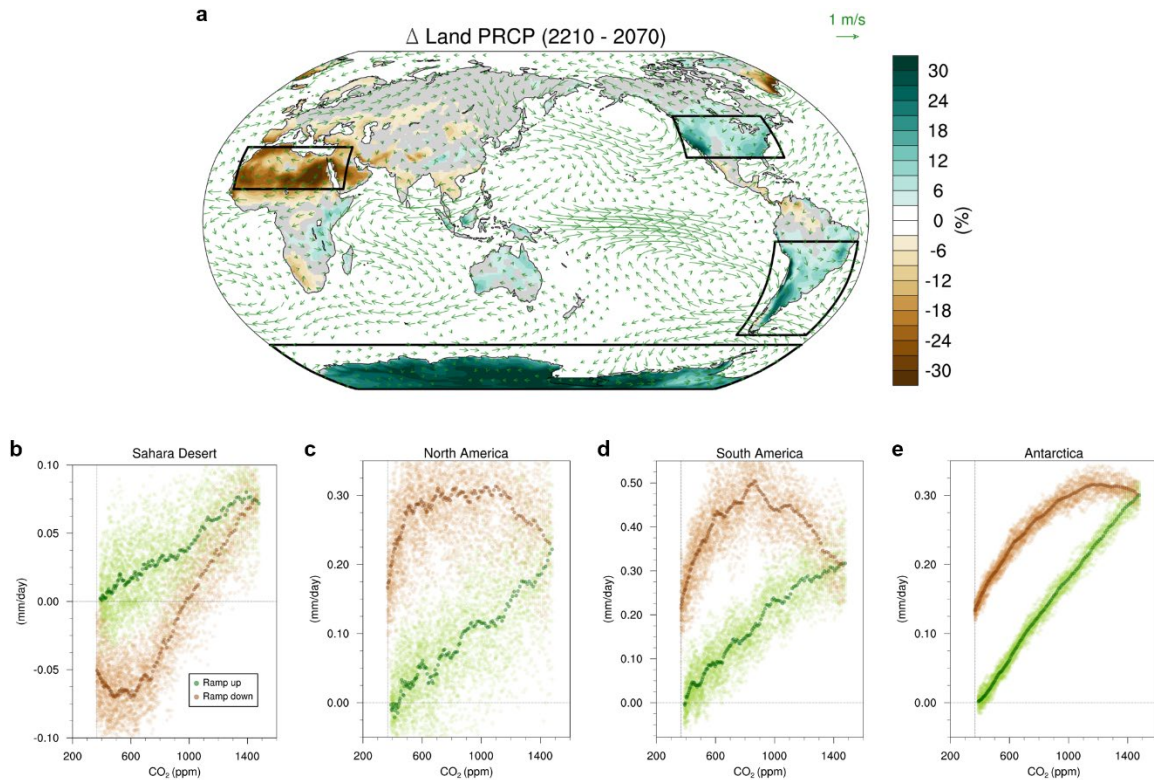
487 **Fig. 1 | Evolution and hysteresis of the temperature, precipitation, and ITCZ**
 488 **location.** Time-series of **a**, CO₂ concentration (green), the global mean surface air
 489 temperature (red), precipitation (blue), and **b**, ITCZ centroid (red). The vertical dotted
 490 lines indicate the maximum or minimum Year of each variable, respectively. The solid
 491 lines and shadings show the ensemble means and the 99% confidence level in the mean,
 492 respectively. (**c to e**) Hysteresis of the global SAT, the precipitation anomalies, and the
 493 ITCZ centroid corresponding to the CO₂ concentration relative to Year 2000. The thick
 494 and light scatters indicate the ensemble means and full ensemble spread, respectively. All
 495 the lines and scatters denote an annual mean and are smoothed by the 11-year running
 496 mean.
 497



498 **Fig. 2 | Changes in the global SAT and hydrological cycle.** **a**, Evolution of the zonal-
 499 mean precipitation anomalies relative to Year 2140. **b**, Difference in the precipitation
 500 between Year 2210 and 2070. **c**, same as **b**, but the data from the CMIP6. (**d** and **e**) same
 501 as **b**, but for the SAT, the precipitation minus the evaporation (shading) and resultant
 502 moisture fluxes (vector). The rightmost shading in panel **e** indicates the zonal mean of the
 503 meridional moisture fluxes. The regions denoted by the cross-shaped dots **a**, colors (**b**, **d**
 504 and **e**), and dots **c**, indicate where the model consistency is insignificant, significant, and
 505 significant, respectively at the 99% confidence level using a bootstrap test. All the
 506 calculations were conducted after taking the 11-year running mean.



507 **Fig. 3 | Changes in the atmospheric meridional energy exchanges.** **a**, Atmospheric
 508 meridional moist static energy flux in the annual mean. **b**, Time-series of the ITCZ centroid
 509 (red), the latitude of the maximum precipitation (blue), the temperature contrast (green)
 510 between the tropics of NH and SH, **c**, the AMOC strength (blue) and the poleward energy
 511 transport at 30°N (red) and 30°S (green). Note that the poleward energy transport at 30°S
 512 is the absolute value. The lines, shadings, and time-filter are the same as in Fig. 1b. (see
 513 Methods for the calculation details)



514 **Fig. 4 | Changes in the land hydrological cycle.** **a**, Difference in the land precipitation
 515 (shading) and 850hPa winds (vector) between Year 2210 and 2070. The precipitation
 516 anomalies are percentage anomalies relative to Year 2070. The regions denoted by colors
 517 indicate where the responses are significant at the 99% confidence level using a bootstrap
 518 test. **b, c, d, e**, Hysteresis of the area-averaged precipitation anomalies relative to Year
 519 2000 in each region, which shows the significant precipitation changes. Sahara Desert
 520 (15°–35°N, 15°W–45°W), North America (30°–50°N, 70°–125°W), South America (10°–
 521 55°S, 35°–80°W), Antarctica (60°–90°S, 180°W–180°E). All the calculations were
 522 conducted after taking the 11-year running mean.

Figures

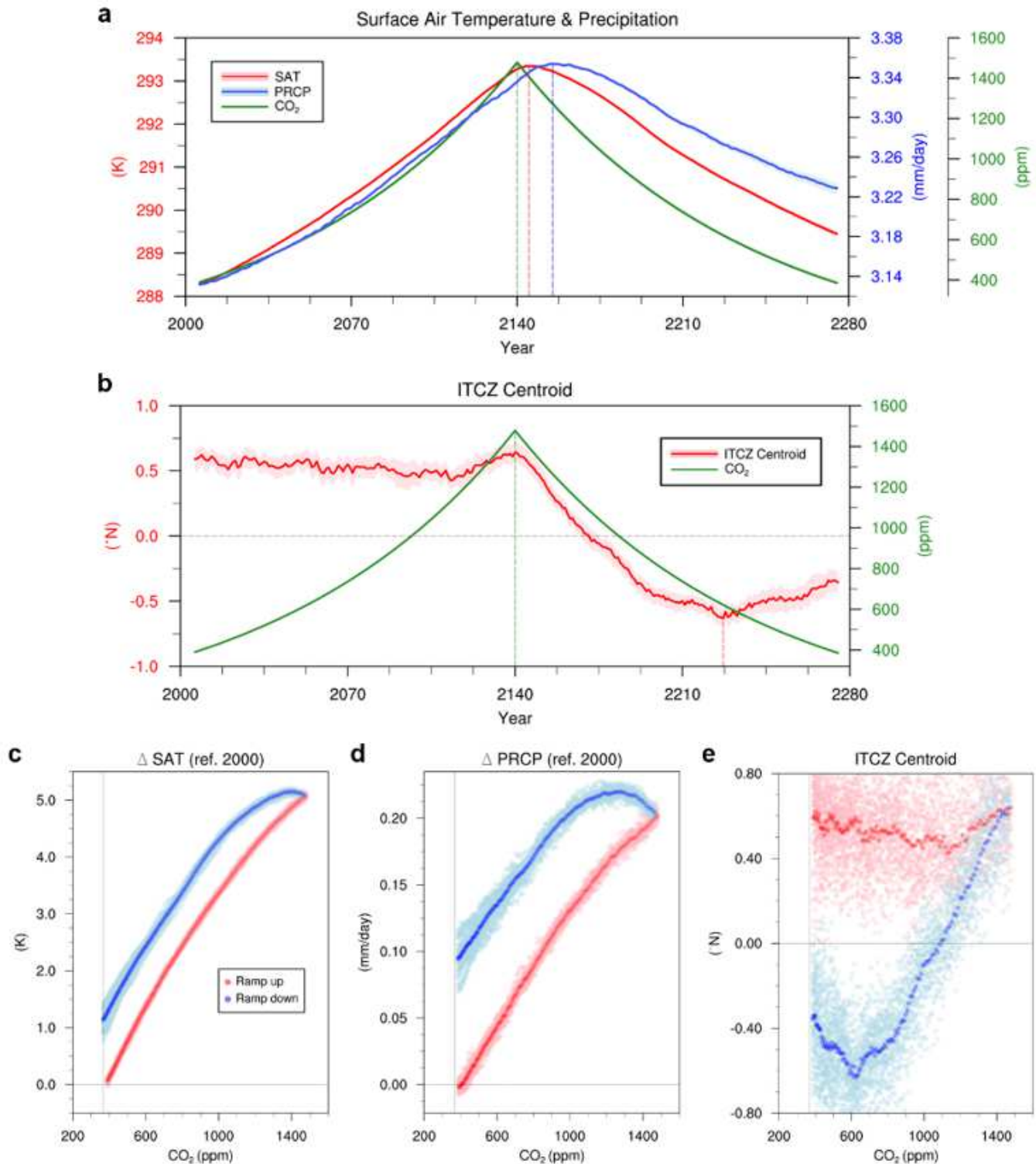


Figure 1

Evolution and hysteresis of the temperature, precipitation, and ITCZ location. Time-series of a, CO₂ concentration (green), the global mean surface air temperature (red), precipitation (blue), and b, ITCZ centroid (red). The vertical dotted lines indicate the maximum or minimum Year of each variable,

respectively. The solid lines and shadings show the ensemble means and the 99% confidence level in the mean, respectively. (c to e) Hysteresis of the global SAT, the precipitation anomalies, and the ITCZ centroid corresponding to the CO₂ concentration relative to Year 2000. The thick and light scatters indicate the ensemble means and full ensemble spread, respectively. All the lines and scatters denote an annual mean and are smoothed by the 11-year running mean.

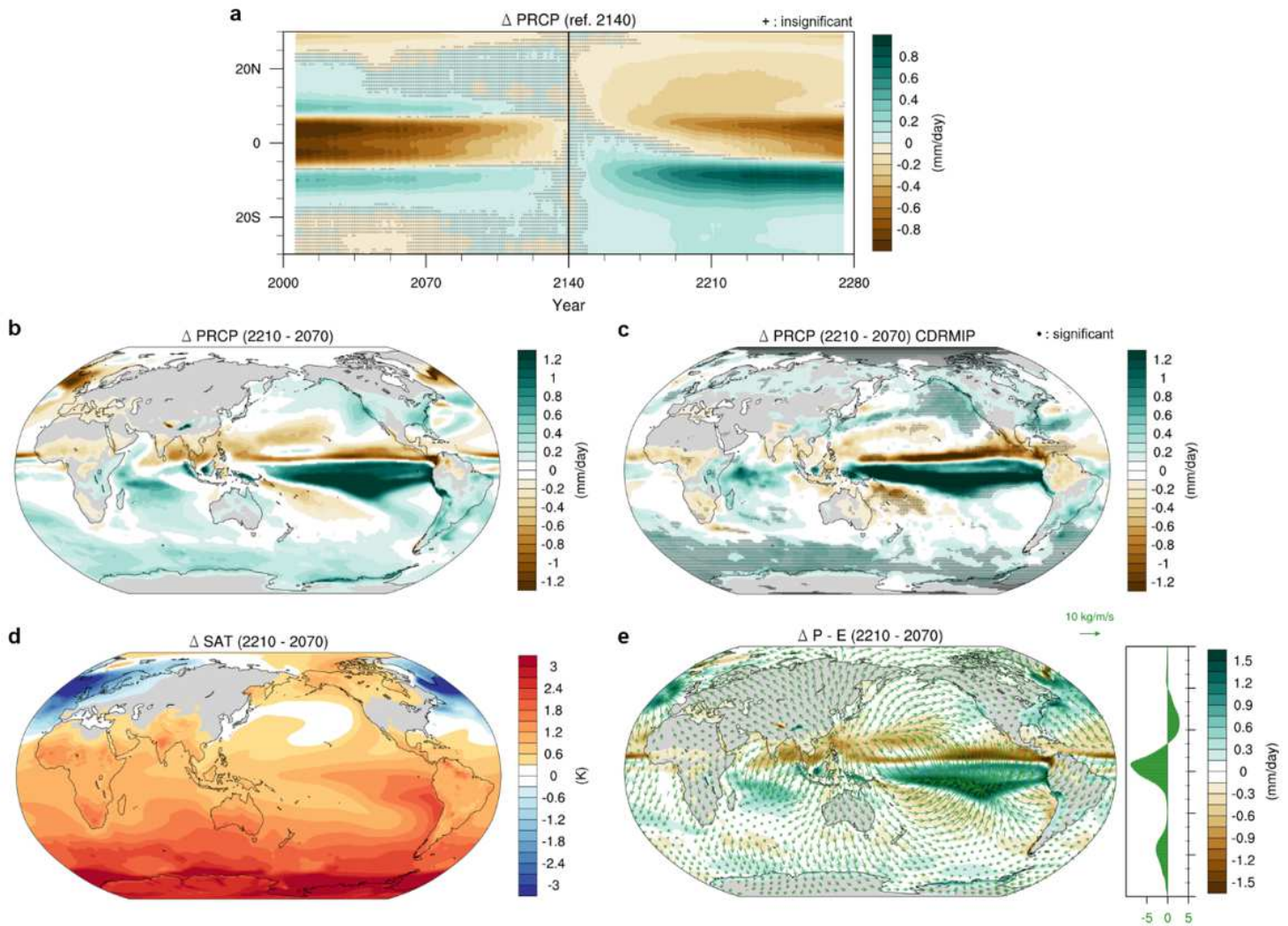


Figure 2

Changes in the global SAT and hydrological cycle. a, Evolution of the zonal-mean precipitation anomalies relative to Year 2140. b, Difference in the precipitation between Year 2210 and 2070. c, same as b, but the data from the CMIP6. (d and e) same as b, but for the SAT, the precipitation minus the evaporation (shading) and resultant moisture fluxes (vector). The rightmost shading in panel e indicates the zonal mean of the meridional moisture fluxes. The regions denoted by the cross-shaped dots a, colors (b, d and e), and dots c, indicate where the model consistency is insignificant, significant, and significant, respectively at the 99% confidence level using a bootstrap test. All the calculations were conducted after taking the 11-year running mean. Note: The designations employed and the presentation of the material on this map do not imply the expression of any opinion whatsoever on the part of Research Square

concerning the legal status of any country, territory, city or area or of its authorities, or concerning the delimitation of its frontiers or boundaries. This map has been provided by the authors.

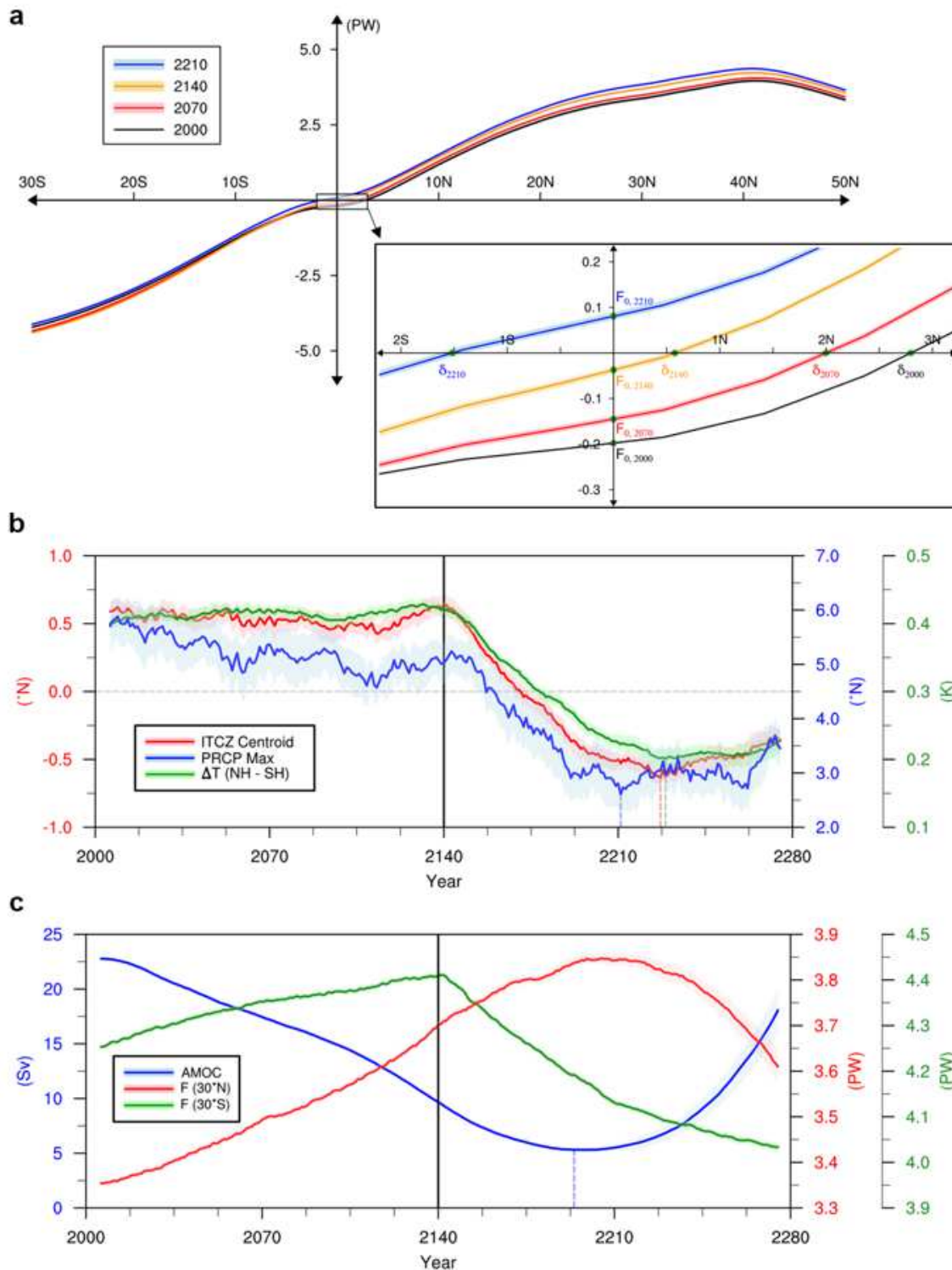


Figure 3

Changes in the atmospheric meridional energy exchanges. a, Atmospheric meridional moist static energy flux in the annual mean. b, Time-series of the ITCZ centroid (red), the latitude of the maximum precipitation (blue), the temperature contrast (green) between the tropics of NH and SH, c, the AMOC

strength (blue) and the poleward energy transport at 30°N (red) and 30°S (green). Note that the poleward energy transport at 30°S is the absolute value. The lines, shadings, and time-filter are the same as in Fig. 1b. (see Methods for the calculation details)

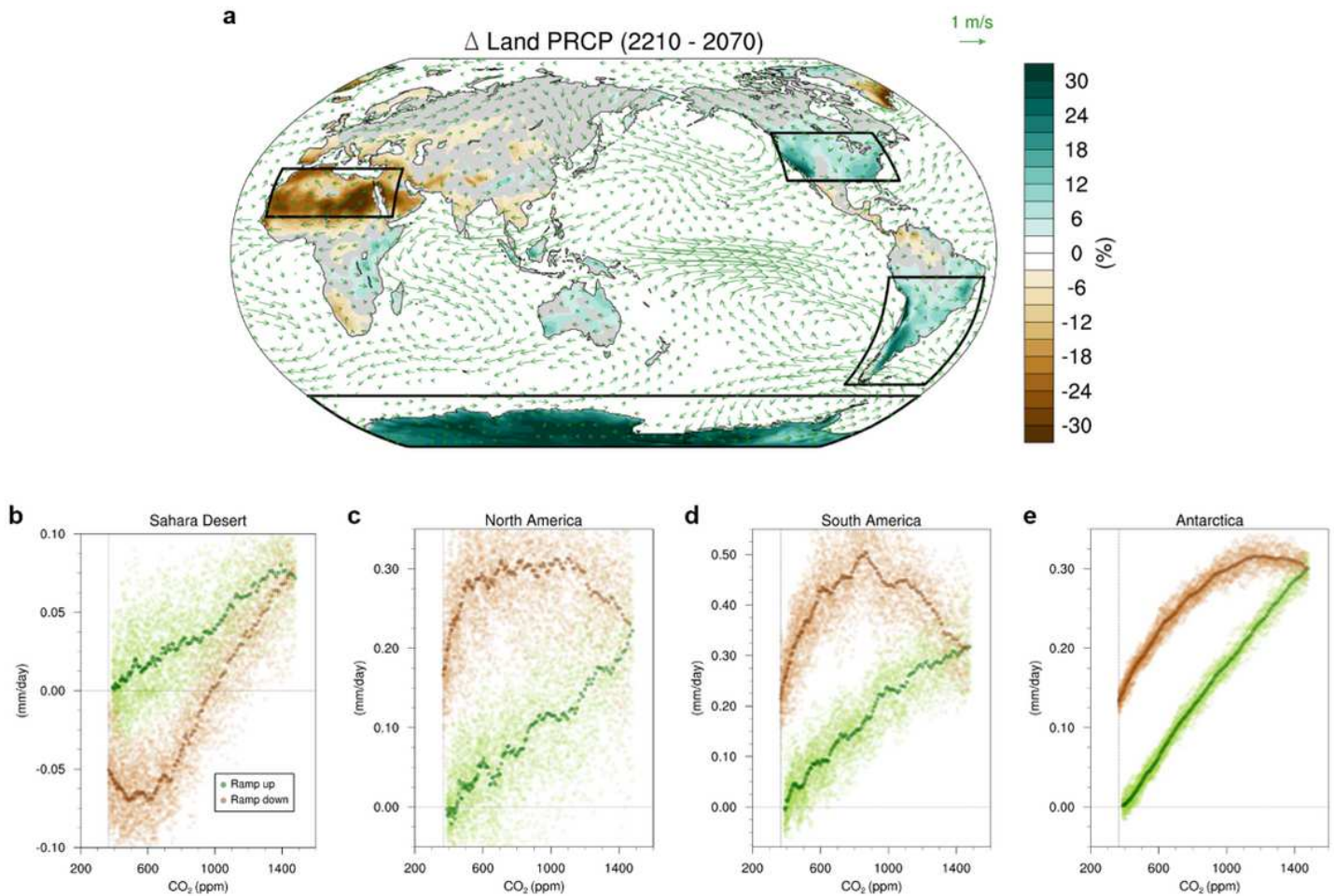


Figure 4

Changes in the land hydrological cycle. a, Difference in the land precipitation (shading) and 850hPa winds (vector) between Year 2210 and 2070. The precipitation anomalies are percentage anomalies relative to Year 2070. The regions denoted by colors indicate where the responses are significant at the 99% confidence level using a bootstrap test. b, c, d, e, Hysteresis of the area-averaged precipitation anomalies relative to Year 2000 in each region, which shows the significant precipitation changes. Sahara Desert (15°–35°N, 15°W–45°W), North America (30°–50°N, 70°–125°W), South America (10°–55°S, 35°–80°W), Antarctica (60°–90°S, 180°W–180°E). All the calculations were conducted after taking the 11-year running mean. Note: The designations employed and the presentation of the material on this map do not imply the expression of any opinion whatsoever on the part of Research Square concerning the legal status of any country, territory, city or area or of its authorities, or concerning the delimitation of its frontiers or boundaries. This map has been provided by the authors.

Supplementary Files

This is a list of supplementary files associated with this preprint. Click to download.

- [ExtendedData.pdf](#)